Additive Manufacturing 35 (2020) 101193

Contents lists available at ScienceDirect

Additive Manufacturing

journal homepage: www.elsevier.com/locate/addma

Research paper

Hot forging wire and arc additive manufacturing (HF-WAAM)

Valdemar R. Duarte[a,*], Tiago A. Rodrigues[a], N. Schell[b], R.M. Miranda[a], J.P. Oliveira[a], Telmo G. Santos[a]

[a] UNIDEMI, Department of Mechanical and Industrial Engineering, NOVA School of Science and Technology, Universidade NOVA de Lisboa, 2829-516, Caparica, Portugal
[b] Helmholtz-Zentrum Geesthacht, Institute of Materials Research, Max-Planck-Str. 1, Geesthacht, 21502, Germany

ARTICLE INFO

Keywords:
Wire and arc additive manufacturing
Directed energy deposition
Forging
Viscoplastic deformation
Stainless steel
Grain refining

ABSTRACT

In this study, we propose a new variant of wire and arc additive manufacturing (WAAM) based on hot forging. During WAAM, the material is locally forged immediately after deposition, and in-situ viscoplastic deformation occurs at high temperatures. In the subsequent layer deposition, recrystallization of the previous solidification structure occurs that refines the microstructure. Because of its similarity with hot forging, this variant was named hot forging wire and arc additive manufacturing (HF-WAAM). A customized WAAM torch was developed, manufactured, and tested in the production of samples of AISI316L stainless steel. Forging forces of 17 N and 55 N were applied to plastically deform the material. The results showed that this new variant refines the solidification microstructure and reduce texture effects, as determined via high energy synchrotron X-ray diffraction experiments, without interrupting the additive manufacturing process. Mechanical characterization was performed and improvements on both yield strength and ultimate tensile strength were achieved. Furthermore, it was observed that HF-WAAM significantly affects porosity; pores formed during the process were closed by the hot forging process. Because deformation occurs at high temperatures, the forces involved are small, and the WAAM equipment does not have specific requirements with respect to stiffness, thereby allowing the incorporation of this new variant into conventional moving equipment such as multi-axis robots or 3-axis table used in WAAM.

1. Introduction

Additive manufacturing technologies have revolutionized the manufacturing industry because of their potential to create complex-shaped structures. For metals, there are several additive manufacturing technologies such as selective laser melting (SLM) and selective laser sintering (SLS) that uses added material in powder form, and wire and arc additive manufacturing (WAAM) that uses added material only in wire form [1]. The first two technologies are used to create parts with good surface finishing, but the production rates are low, whereas in WAAM, the deposition rate is high at the expense of surface smoothness. This variant is more adequate for the production of large parts.

WAAM is based on multiple-pass welding and its metallurgy [2]; thus, the microstructure of the parts consists of coarse columnar grain structures [3] as a consequence of the successive re-melting and solidification thermal cycles. Aside from a large grain size, the mechanical resistance is low and anisotropic due to which premature failure of the component can occur under multi-axial tensile or cyclical solicitations.

Another potential detrimental feature is the formation of pores [4]. In this case, the existence of pores in parts to be used in structural applications can be critical because a significant decline in the mechanical properties of the parts depending on their volume fraction and location may be observed. This is also a major concern for non-destructive testing (NDT) [5] that may not ensure the detection of such defects.

One crucial step to the industrialization of Additive manufacturing is the application of non-destructive testing (NDT), which have been facing many challenges due to the complex geometry and high surface roughness of the additively manufactured parts [5].

Recent developments in this topic have shown the potential of computed tomography (CT) and ultrasonic testing. However, CT could be expensive and presents several limitations regarding the application of NDT in situ. Ultrasonic (UT) methods, particularly, phased array ultrasonic testing, had proven to be a feasible technique in the inspection of AM parts, with high reliability and sensitivity [6,7]. Yet, this technique requires a plane surface, commonly achieved by machining, to assure the probe correct coupling. With the presented variant, the top surface of the sample is flat, which facilitates the coupling of ultrasonic

* Corresponding author.
E-mail address: v.duarte@campus.fct.unl.pt (V.R. Duarte).

https://doi.org/10.1016/j.addma.2020.101193
Received 12 February 2020; Received in revised form 26 March 2020; Accepted 29 March 2020
Available online 28 April 2020

and eddy currents probes without the need of post processing.

The existence of both large grain structures and pores has motivated researchers to find methods to minimize, or even eliminate, these microstructural features. One way to decrease grain size and porosity simultaneously is through the application of pressure between the deposited layers. Colegrove et al. [8] first applied interpass cold rolling after the deposition of each layer. To achieve effective grain refinement, a load between 50 and 75 kN was required because rolling was only applied when the material was almost at room temperature (≈50 °C), and cold plastic deformation was intended to produce a hardening effect on the material. When the following layer was deposited, the heat transferred to the previously deformed material induced recrystallization of the grain structure. Although this method is effective in reducing the grain size and collapsing pores that may exist within the deposited layer [4], it is time-consuming because it is necessary to wait for the material to cool down before rolling. Zang et al. [9] developed a hot-micro-rolling tool that follows the welding torch movement, forging the welding bead above 800 °C layer by layer. Yang et al. [10] developed a hot-rolling tool consisting of three rolls that were able to deform simultaneously the three sides of any deposited layer with an applied rolling force of 3 kN. Both studies revealed improvements in the dimensional accuracy and mechanical properties of the produced parts. However, these methods involve the production of an entirely different additive manufacturing equipment with high structural stiffness. This prevents the use of a commonplace welding source and a robot or an XYZ table, and it increases the cost of the process, thereby making it less competitive.

The application of surface treatments, such as laser shock peening and ultrasonic peening, have also been studied [11]. These treatments have proven to reduce residual stress and refine the microstructure. However, comparing with the rolling methods, these processes are less efficient to improve the geometrical accuracy of the part.

In this study, we propose a new WAAM variant to achieve a similar effect while avoiding down times between layers deposition and reducing the required load for deforming the material: it encompasses performing a locally viscoplastic deformation of the already deposited layers immediately after the material is deposited. Such a process would resemble semi-solid forging [12]. By deforming the as-deposited layer at high temperature, it is possible to induce dynamic recrystallization of the material and promote the collapse of pores that may have formed during the deposition. These two features can be achieved under a fraction of the load required if the deformation is performed at low temperatures, i.e., near room temperature.

The presence of recrystallized grains in WAAM parts has several apparent advantages: first, it can increase the mechanical strength following the Hall–Petch relationship; then, the existence of refined grains at the top of the deposited layer provides a higher density of nucleation sites, thereby decreasing the susceptibility to large grain growth as observed in WAAM deposits. This is particular relevant for alloys without solid state transformations, more susceptible to large grain growth during successive thermal cycles. Another potential advantage of deforming the as-deposited layers at high temperature is to improve the waviness and surface roughness, thereby increasing part accuracy and reducing material waste upon subsequent machining processes.

In this study, a novel WAAM variant designated hot forging wire and arc additive manufacturing (HF-WAAM) is presented. The process fundamentals and its effects on the microstructure of a full austenitic stainless steel part are presented and discussed. It is expected that this new process can be used to improve the microstructure and mechanical properties of the deposited material. Thus, since there is no need to wait for the material to cool down to near room temperature this variant can be applied without an increase in the production time, which is known to occur when cold rolling variant is applied.

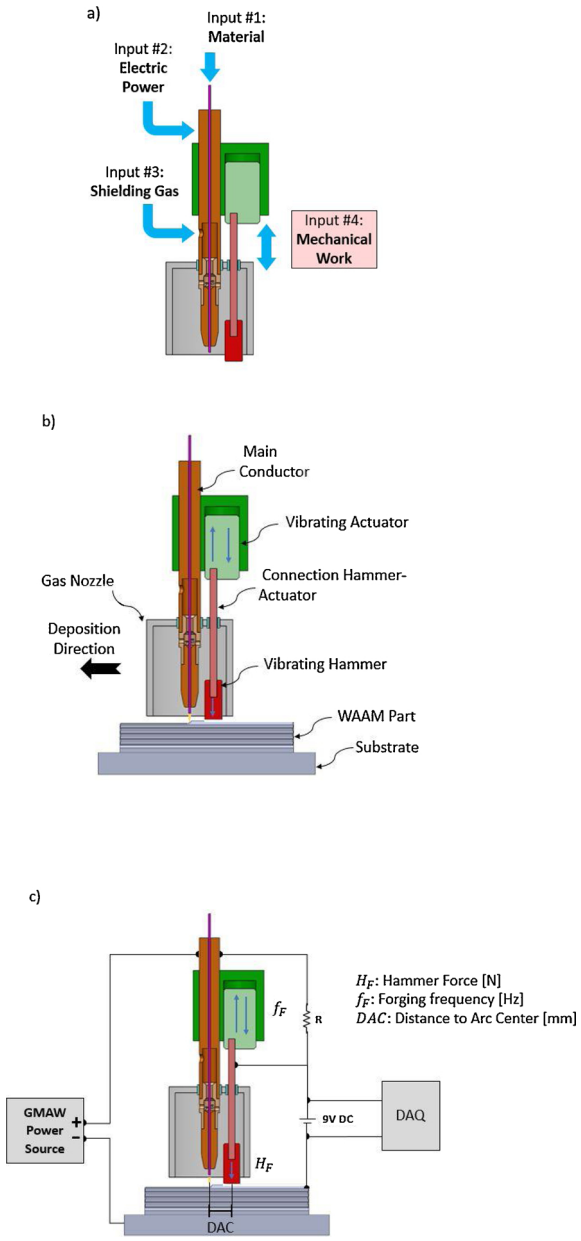

Fig. 1. Schematic representation of a) HF-WAAM inputs, b) HF-WAAM components, and c) process parameters and electrical scheme used to avoid arc between the vibrating hammer and welding torch.

2. Process fundamentals

Most of the researchers currently working on WAAM are using conventional welding torches attached to a moving equipment, which is usually a 6-axis robot arm. Conventional welding torches were designed to be used by an operator; the power, shielding gas, and wire are fed through the same hose because of ergonomic and safety concerns. Under such design constraints, these torches are impractical for a WAAM application. Therefore, we propose an innovative concept of a multi-feed device wherein the different inputs are decoupled and can be controlled independently; these include the electrical power, shielding gas, material feed, and a new input consisting of mechanical work/locally viscoplastic deformation (Fig. 1a).

The main objective of HF-WAAM is to utilize the viscoplastic deformation behavior at high temperatures to reduce residual stresses, increase ductility, eliminate post-heat treatment operations, and homogenize grain structure. This innovative technology allows the

reduction of the forging load, tooling, and equipment stiffness. In the overall, HF-WAAM involves the use of a hammer placed inside the gas nozzle, which is activated by a vibrating actuator (Fig. 1b). The vibrating actuator can be electromagnetic (solenoid) or mechanical (pneumatic cylinder), and it can operate at different frequencies. The hammer travels along with the torch and is activated while the material is still being deposited; the part is forged at temperatures close to 900 °C, which exceed the recrystallization temperature for this material (≈450 °C); this is similar to a hot forging process, and deformation and solidification occur.

Certain elementary electrical precautions must be considered. The welding nozzle is electrically isolated from both the main conductor (+) and the part (−) as in gas metal arc welding (GMAW) torches. Additionally, the vibrating hammer is electrically connected to the main conductor (+) through a high electrical resistance (R) (Fig. 1c). Thus, when the hammer is lifted but remains very close to the WAAM part, its electrical potential is the same as that of the main conductor (+), thereby avoiding arc ignition between the two. In addition, the high electric resistance (R) also avoids the current flow from the part to the hammer when a short circuit is established due to the hammer contacting the part.

Other hammer geometries or component assemblies that can be considered for HF-WAAM include: i) a hammer with a circular crown geometry concentric with the wire, ii) a hammer outside the gas nozzle, and iii) the gas nozzle itself as a hammer. The last two allow the HF-WAAM to be applied in nonlinear deposition paths because the forged area can fully rotate 360°, and to apply this variant to multi beads fabrication. Furthermore, the hammer might be designed in order to reduce the part waviness and increase the geometric accuracy.

HF-WAAM introduces an additional set of process parameters (Fig. 1c) that may influence the final metallurgic, mechanic, and geometric properties of the part. This set includes the following parameters: forging force, F_F [N]; forging frequency, f_F [Hz]; distance to arc center, DAC [mm]; hammer geometry. The area forged in each cycle depends on the bottom surface geometry of the hammer and on the forging step, F_s [mm] that is the distance traveled by the hammer in one cycle; this is a function of f_F and travel speed, $V_{deposition}$ [m/s]. Thus, the forging step is given by the following equation:

$$F_s = \frac{1}{f_F} \times V_{deposition} \tag{1}$$

For a cylindrical hammer, the forging step must be lower than the hammer radius to avoid leaving unforged areas between steps. To determine the applied pressure, it is necessary to identify the area forged during each cycle. For this particular geometry, the area forged is represented in Fig. 2 and can be estimated by Eqs. (2)–(4).

$$A = F_s \times l_w \tag{2}$$

$$l_w = \frac{2\pi R_m \times 2\beta}{360} \tag{3}$$

$$\beta = \sin^{-1}\left(\frac{W}{2R_m}\right) \tag{4}$$

Where: R_m [mm] is the hammer radius, l_w [mm] the arc length, W [mm] the bead width, and β [°] the angle of the arc half-length.

3. Materials and methods

A customized WAAM torch (Fig. 3) was attached to a moving head within a working envelope of 2760 × 1960 × 2000 mm^3. A *PRO MIG 3200* power source from *KEMPY* was used to deposit a 1 mm diameter AISI316L stainless steel on a mild steel substrate. Two pneumatic cylinders were used as vibrating actuators: a *FESTO ADVC-6-5-A-P* with a produced force of 17 N at 0.6 MPa and an *SMCCU10-10T* with a produced force of 55 N at 0.6 MPa. Both the pneumatic cylinders were connected to the tool steel hammer by an M6 leadscrew. A 5/2-way bistable solenoid valve *Festo VUVS-LK20* controlled by a data acquisition (DAQ) device was used to actuate the pneumatic cylinders.

The length of the produced samples was fixed at 100 mm and the time interval between depositions was fixed at 2 min. A one-way deposition strategy was adopted, wherein the torch always returned to the same starting point. Four samples were produced to study the effect of HF-WAAM: one as-built sample and three samples with forging forces of 17, 55 N. The first two hot-forged samples were produced using a cylindrical hammer of diameter 10 mm, and the last one was produced using a parallelepiped-shaped hammer of contact area 3 × 9 mm^2. To prove its effectiveness in reducing the number of pores, the same samples were reproduced without shielding gas. The process parameters used to deposit and deform the material are shown in Table 1. It should be noticed that the hammer force is prescribed by a pneumatic actuator and therefore, the applied force remains constant along the part since the compressed air remain at constant pressure during the entire process.

An electrical circuit was set up to evaluate the intermittent contact between the hammer and the part. The circuit uses a 9 V battery to create a current loop and make the hammer act as a switch when it comes in contact with the part (Fig. 1c). Therefore, it is possible to identify the contact period (short circuit/low voltage) and the non-contact period (open circuit/maximum voltage) by using a DAQ device to measure the battery voltage. Fig. 4 depicts the hammering effect during a time interval of 1 s; a hammering frequency of 10 Hz and a duty cycle of approximately 48 % are confirmed.

A *Fluke TI400* thermographic infrared camera was used to monitor

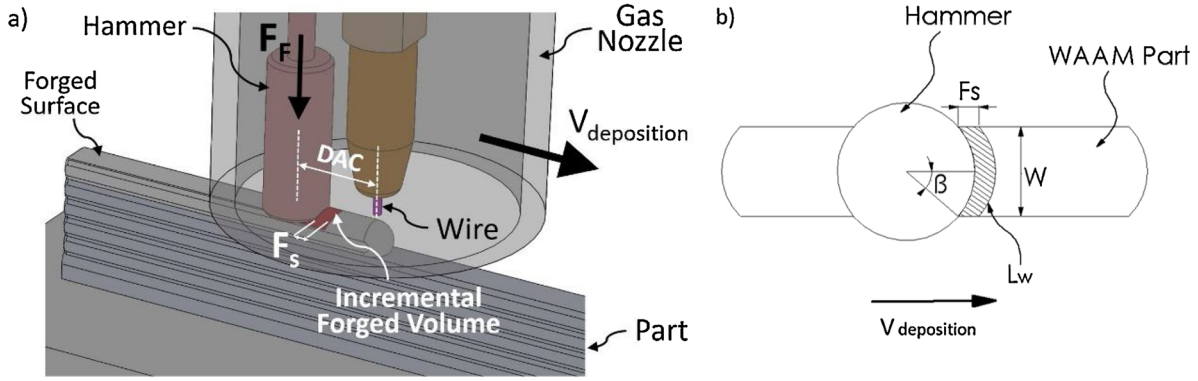

Fig. 2. Schematic representation of the forged area at each step: a) isometric view (3D); b) top view (2D).

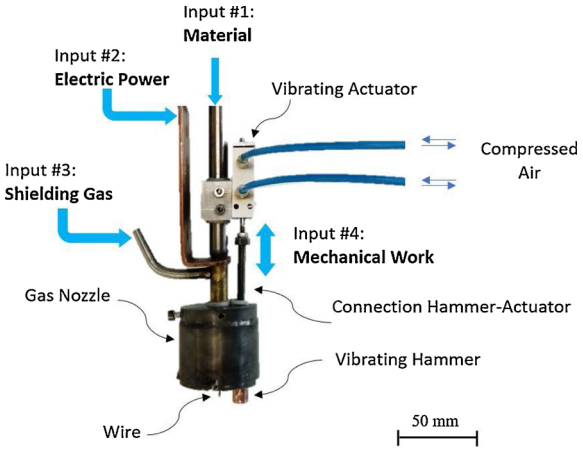

Fig. 3. Customized hot forging wire and arc additive manufacturing (HF-WAAM) multi-feed device.

Table 1
Process parameters used during HF-WAAM.

Welding mode	Gas metal arc welding – continuous mode (DC+)
Number of layers	10
Forging frequency	10 Hz
Distance to arc center	14 mm
Wire feed speed	4 m/min
Travel speed	360 mm/min
Voltage	20 V DC
Contact tip to work distance	6 mm
Shielding gas	Argon 99.99 %
Gas flow rate	12 L/min

the temperature of the parts during fabrication. The camera had an accuracy of ±2%, a measurement limit of 1200 °C, a refresh rate of 9 Hz, and a resolution of 320 × 240 pixel. The emissivity of 0.7 was validated using thermocouples. The temperature was measured at any point during the buildup using the acquisition software *SmartView*.

Cross-sections from the center of each sample were cut, polished, and etched with *Vilella's reagent*. The metallographic analysis was conducted using a *Leica DMI 5000M* inverted optical microscope. The geometric properties of the parts were measured using the image software *Adobe Photoshop CS6*.

X-ray diffraction was performed at beamline P07 High Energy Materials Science (HEMS) of Petra III/DESY, using a wavelength of 0.1426 Å (87.1 keV) and an incident beam of 1 × 1 mm. A Perkin-Elmer detector, with a pixel size of 200 × 200 µm, was placed at 1.40 m from the sample. LaB_6 powder was used for calibration. The raw 2D Debbye-Scherrer images provide qualitative information on the grain size and texture of the analyzed material [13].

Uniaxial tensile tests were performed on an Autograph Shimadzu machine model AG500Kng equipped with a Shimadzu load cell SFL-50kN AG with a total capacity of 50 kN. A crosshead displacement speed of 0.01 mm/s was imposed, and the tests were performed at room temperature. Specimens for uniaxial tensile testing were obtained in the vertical direction from the as-built and 55 N hammered samples. Three specimens for each condition were evaluated to assess the reproducibility of the parts mechanical properties. The fracture surfaces of both as-built and hot-forged samples were analysed by a TM3030 Plus Voltage Tabletop Scanning Electron Microscope (SEM) at an acceleration voltage of 15 keV.

4. Results and discussion

Fig. 5 shows the samples fabricated with different forging forces, hammer geometries, and shielding gas flow rates. The samples were intentionally repeated without the use of shielding gas to promote the formation of pores, and thus characterize the feasibility of the hot forging variant in collapsing and reducing porosity in the produced parts. The differences in height between the beginning and end of the deposition for the one-way deposition strategy occurs due to rapid cooling and the small amount of heat accumulated at the beginning of the deposited layer, in contrast to the large amount of heat accumulated at the end of each deposited layer. This needs a correction of the processing parameters by the software. It is evident that the hammer has a considerable impact on the bead geometry as it flattens the layers along its length, thereby diminishing this feature that needs inline parametric correction. The flat top surfaces in this variant are achieved due to the constant process conditions where hammering is applied. Since deformation is occurring always at the same distance of the electric arc, the material temperature and, therefore, its properties will be the same. This means that by keeping the force constant throughout the process will result in even flat surface as shown. Furthermore, the forging step in the deposition was of 0.6 mm, which means that at each stroke the hammer advances 0.6 mm. Since the hammer has a diameter of 10 mm, the remaining length (9.4 mm) acts as a limiter, promoting a continuous height along the deposition direction.

The effects of hot forging are visible in the macrographs of the cross-sections removed from each sample produced with shielding gas (Fig. 6). With hot forging, the layers became larger and thinner when increasing the forging forces, and this is particularly evident for the sample produced with the rectangular hammer. This is explained by the reduced contact area of the rectangular hammer (27 mm^2) compared to the one with a circular shape (78.5 mm^2). By reducing the contact area, the stress increases; consequently, the deformation increases. Another observation is the flattening effect of the last deposited layer that assists deposition of the subsequent layer.

The width and height of each part were measured. The respective average and standard deviation values are shown in Fig. 7. The part dimensions are compared to the control specimen. The height of the parts decreases with increase in the forging force, and the width

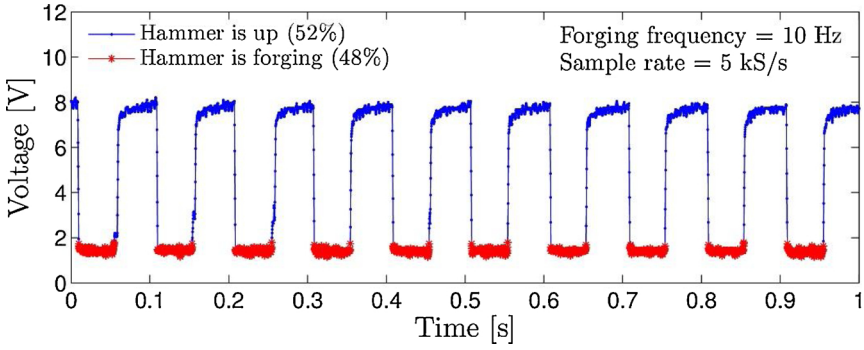

Fig. 4. Variation of voltage with respect to time to detect hammering during deposition.

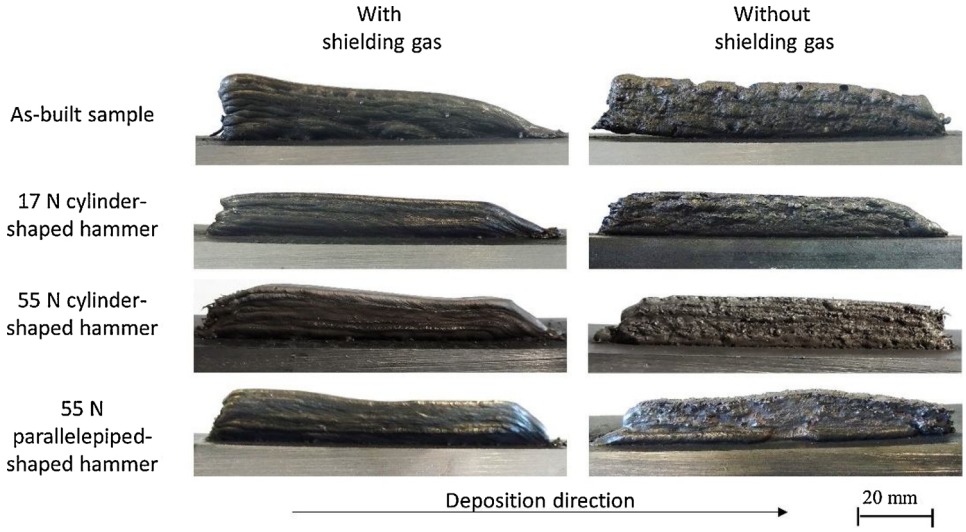

Fig. 5. Overall aspect of the samples produced with different process parameters.

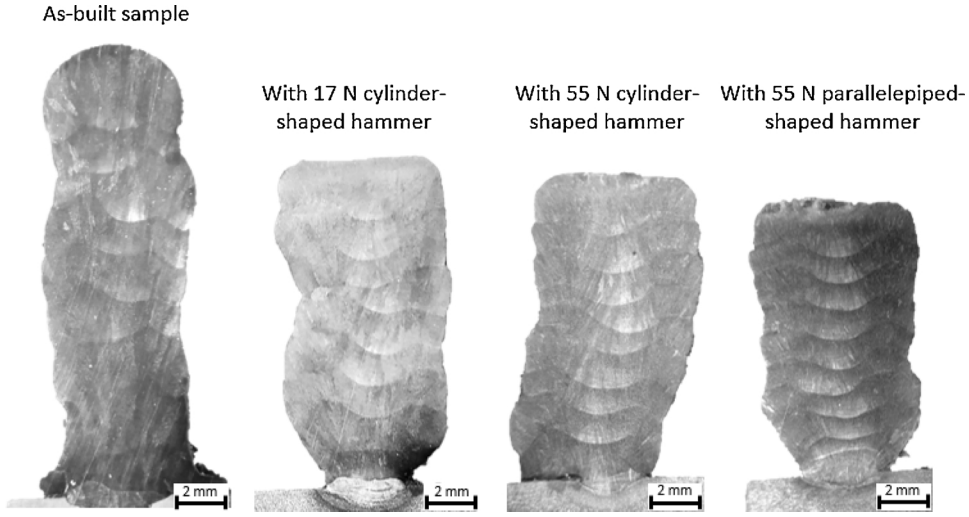

Fig. 6. Cross-section of the samples produced with shielding gas.

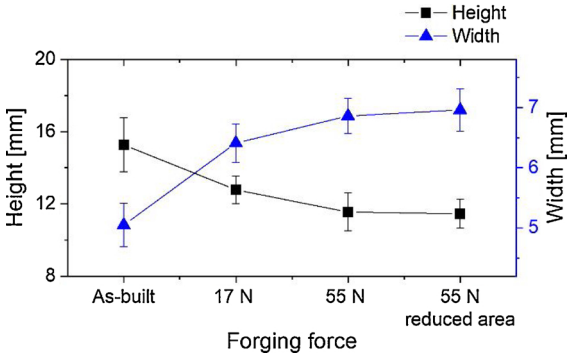

Fig. 7. Height and width measurements of each produced sample.

increase because of volume conservation in plastic deformation domain.

The thermal field analysis during material deposition was used to determine the temperature of the material while it is being forged, and the temperature of the hammer during this process. Fig. 8 depicts a thermographic image acquired during the deposition of one layer of a sample produced with a cylinder-shaped hammer under a load of 17 N. As it can be seen, the material under the hammer is at a temperature of

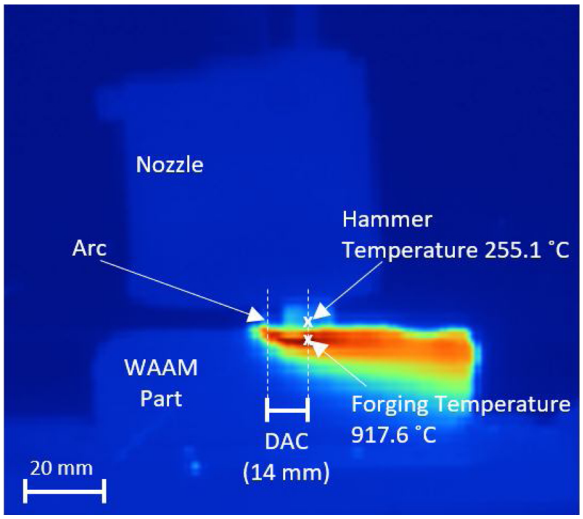

Fig. 8. Thermographic analysis of the deposited layer during forging process.

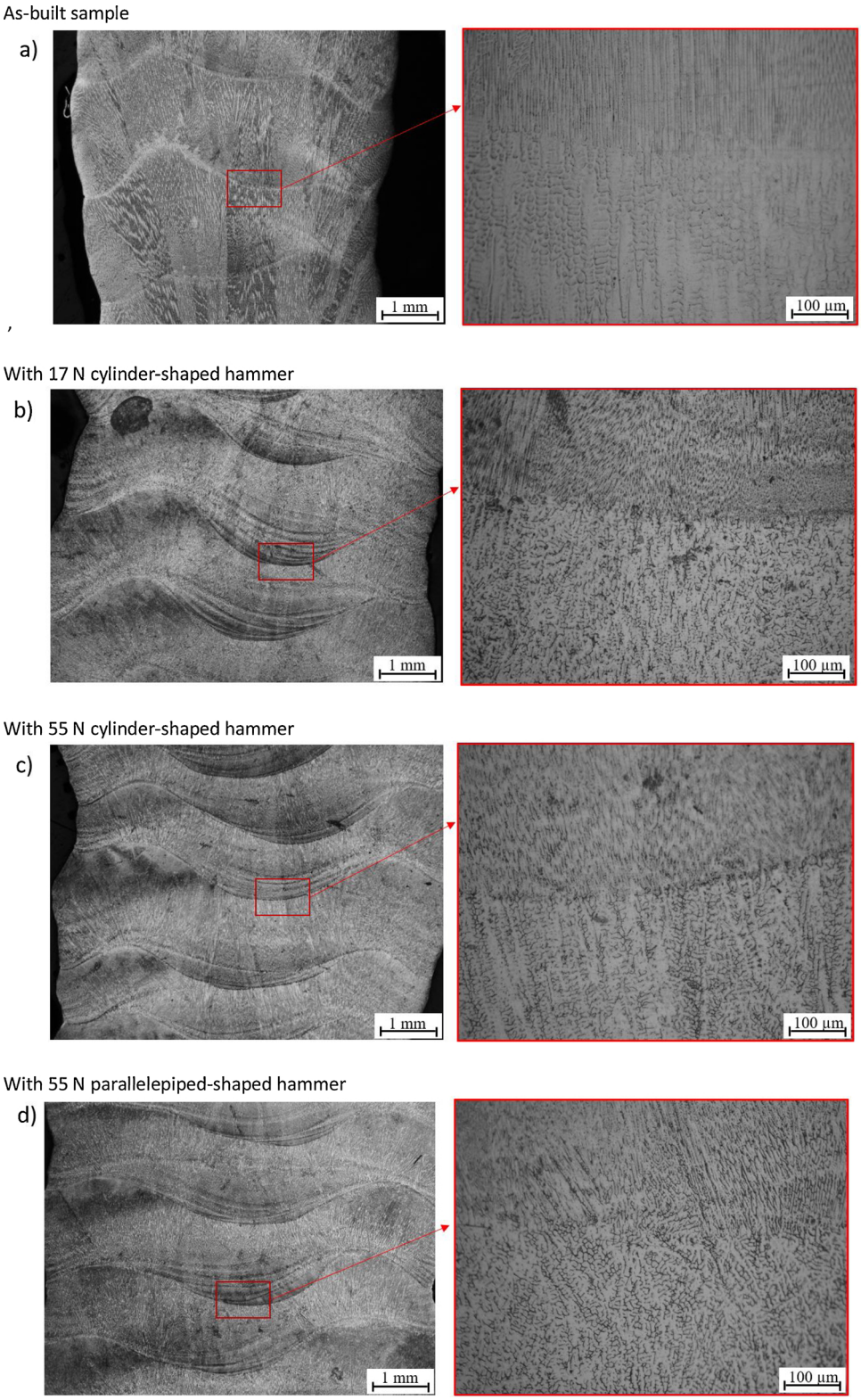

Fig. 9. (a) Micrographs of the as-built, (b) hot-forged with 17 N cylinder-shaped hammer, (c) hot-forged with 55 N cylinder-shaped hammer, (d) hot-forged with 55 N parallelepiped-shaped hammer.

about 917 °C, while the hammer is at 250 °C. At these temperatures, the austenitic stainless steel 316 L shows strain hardening, strain rate hardening, thermal softening and coupled effect of temperature and strain, since it is in the range of hot working conditions (800–1200 °C) [14]. Looking to the hammer temperature, since it is made of tool steel the temperatures reached are insufficient to damage or soften it. Thus, this thermal analysis allows to confirm that the hammer actuates on the material while it is still at temperatures in the range of hot working operation, which can potentially improve the mechanical properties of the deposited material.

The grain size and morphology are determined by the solidification conditions during the liquidus/solidus transformation. In non-

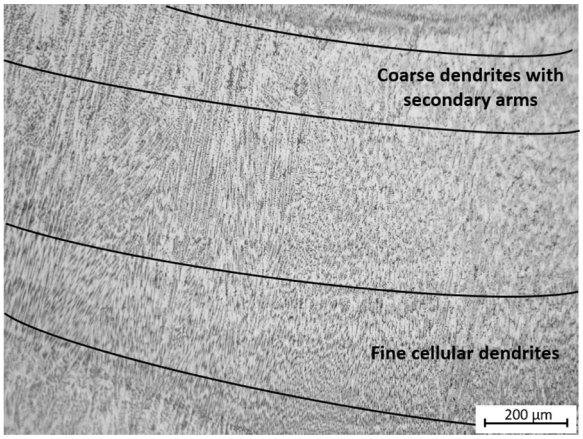

Fig. 10. Micrograph of the as-built sample, in which regions with fine and coarser dendrites developed within a single deposited layer are highlighted.

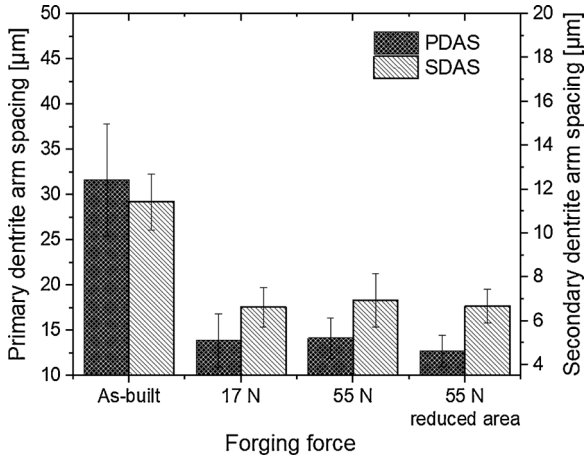

Fig. 11. Primary dendrite arm spacing and secondary dendrite arm spacing measured in each sample.

equilibrium solidification, as observed in additive manufacturing, the parameters that mostly affect the solidification microstructure include the temperature gradient (G), solidification rate (R), undercooling (ΔT), and alloy composition [15]. In WAAM of 316L stainless steel, a cellular or columnar dendritic structure is commonly observed that occurs when G is low and/or R is high [16]. A dendritic structure grows in the opposite direction of the temperature gradient and is perpendicular to the isotherms.

Fig. 9 shows optical micrographs of transverse sections of each sample and the presence of δ ferrite in the interdendritic spaces of primary austenite (γ) dendrites. These phases are a result of high cooling rates that shorten the cooling time and limit the diffusion-controlled transformation from δ to γ phase [16]. The micrographs also show a significant difference of the dendrites size in the region between two consecutive layers, as well as a decrease in grain size in the samples where forging was applied.

On the as-built sample, each layer presents a fine cellular dendritic structure at the bottom, which develops into a coarse dendritic structure with secondary arms near the fusion line at the top of the layer (Fig. 10). This grain growth pattern is observed in each layer.

In WAAM, the cooling rate decreases from the bottom to the top of the layer, which promotes a finer microstructure at the bottom, due to the insufficient time to form dendrites with secondary arms, and a coarser one at the top [17]. Additionally, the top region of each layer is refined by the subsequent layer.

In the hot-forged samples, the grain structure was observed to have the same growth pattern with fine cellular dendrites at the bottom and a coarse dendritic structure at the top of each layer.

With *Image J* software, the dendrite arm spacing measurements were performed in groups of 5 consecutive dendrites arms and the obtained value divided by five. The methodology was repeated 7 times in order to obtain an average and standard deviation value for each analyzed sample.

From the comparison of both secondary and primary dendrite arm spacing, (SDAS) and (PDAS), respectively, it is seen that HF-WAAM produced a finer solidification structure with smaller primary and secondary dendrite arm spacings (Fig. 11). Relationships between grain size and yield strength, such as Hall-Petch's equation, indicate that a decrease in grain size causes an improvement in mechanical properties. It has been observed that HF-WAAM is effective in the reduction of grain size and thus it might improve the mechanical properties of the parts.

In HF-WAAM, grain refinement due to forging causes the presence of more heterogeneous nucleation sites, which promotes competitive grain growth. As a result, upon solidification, more grains form and the grain size of the layer is reduced. It is interesting to note multiple lines delimiting each layer on the HF-WAAM samples. These are due to the pulsed hammer effect during layer deposition (Fig. 12). The high temperature plastic deformation induced by the HF-WAAM variant results in a grain refinement effect, which in turn contributes to increase the strength of the as-built parts. These results are in good agreement with the Hall-Petch equation, which states that smaller grain size, as that obtained after HF-WAAM is applied, results in a higher mechanical strength, as evidenced in the tensile tests depicted in Fig. 14.

The 2D Debbye-Scherrer diffraction rings of the as-built and hot forged samples are depicted in Fig. 13. By analyzing the Debye-Scherrer Rings of the as-built sample, "spotty" diffraction rings with intensity reinforcements at different azimuthal angles are visible. This is evidence of a material with a large grain size and/or a strong texture. Both the large grain size and strong texture occur in the as-built sample since

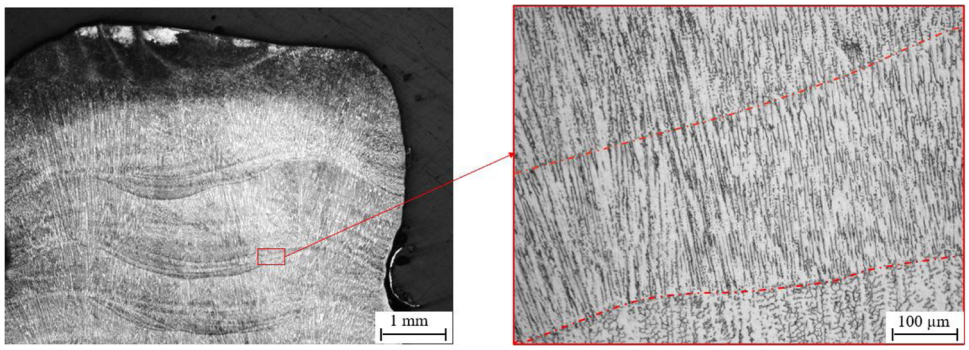

Fig. 12. Micrograph showing grain growth discontinuities (dash lines) in the hot-forged samples.

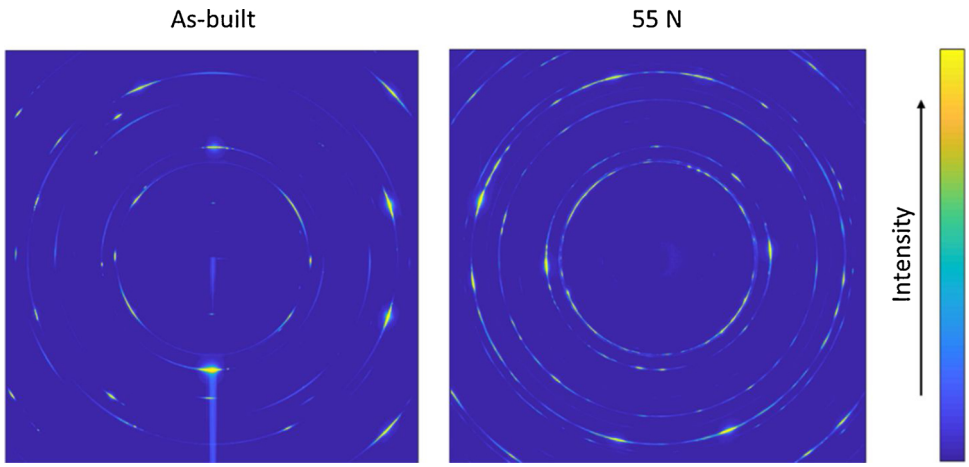

Fig. 13. 2D Debbye-Scherrer diffraction patterns of the as-built (left) and hot forged (right) samples.

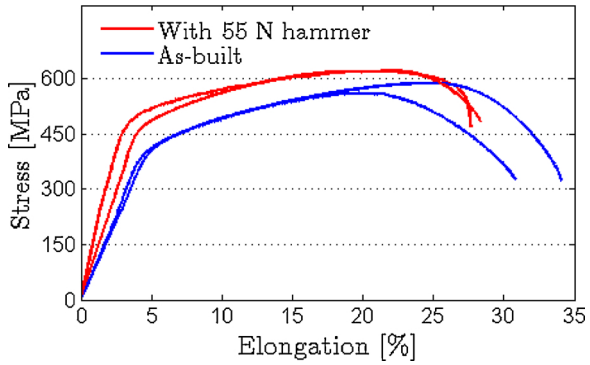

Fig. 14. Uniaxial tensile Stress-Elongation curves for the as-built and 55 N hammered samples.

the solidification microstructure is continuous (columnar grains) along the height of the wall. Opposite to this, in the hot forget sample, continuous diffraction rings are observed, evidencing a decrease in grain size (in good agreement with the microscopy images) and no significant texture effects are observed. The effect of the hot forging process in refining the grain structure promotes more nucleation sites for solidification to occur at a given deposited layer which, in turn, decreases the grain size and modifies the solidification texture of the material.

To evaluate the mechanical properties of both the as-built and 55 N hammered parts, tensile tests until fracture were performed. Representative stress-strain curves are depicted in Fig. 14. The samples average values for the ultimate tensile strength (UTS) were of 574 and 622 MPa, for the as-built and hot forged parts, respectively, while the elongation varied from 32.5 to 27.9 %. The samples produced with the hot forging exhibited in average an increase in the UTS of 8.6 % and a decrease of 13.9 % in the elongation. Additionally, the yield strength increased from 360 to 450 MPa with the application of hot forging during the deposition. As mentioned above, the hot forging promotes a grain size reduction which increases the amount of grain boundaries that difficult the dislocation slip, and increase the material strength. According to the Hall-Petch equation, smaller grain size translates into higher mechanical strength [18]. As such, the refinement effect induced by the HF-WAAM variant is the strengthening mechanism in the produced parts. It should also be mentioned that the results also show an increase in the UTS is accompanied by a decrease of elongation, a measure of the ductility, which is again in good agreement with the effect of grain size on the mechanical properties of most engineering materials [19]. Nevertheless, it must be emphasized the small loss of ductility observed, which does not prevent the use of AISI316L steel in most industrial applications where ductility is required.

The fracture surfaces observed by SEM of the as-built and 55 N hammer are depicted in Fig. 15. Fractography analysis reveals that both specimens have a ductile fracture, consisting of well-developed dimples over the entire fracture surface. The average dimple diameter of both samples was measured. The results shown an average reduction from 2.4 μm, in the as-built sample, to 1.2 μm in the 55 N hammer sample. These results further evidence that this new hot forging WAAM variant promotes a grain size reduction resulting in an increase of the grain boundary density and thus improved mechanical properties.

Contamination of the part by the hammer was not verified when optical microscopy, scanning electron microscopy and x-ray diffraction were performed."

It is well known that the shielding gas is always necessary in electric arc-based welding processes for several reasons, amongst these is avoiding the formation of pores. In this study, we intentionally did not use shielding gas to promote the formation of pores, as described in the experimental procedure. The hot forging variant of WAAM was observed to reduce the number of pores and their locations in the central zone. Fig. 16 presents optical images of non-forged samples produced without gas. It is evident that the pores develop through several layers and some are located at the central zone of the cross-sections.

In the parts manufactured with the hammer (Fig. 17) the pores are almost collapsed and are displaced to the periphery, reducing their number and size with the increase of the forging force. Owing to the normal curvature of the as-built beads, the central zone is the first to be deformed, such that the pores tend to move to the borders. Because most of the WAAM-fabricated parts must be machined to the required surface finishing, a subtractive process may enable the elimination of all the porosity located in the lateral subsurface of the part.

With the increase in the forging force, the sphericity of the pores changes and these become oval. Moreover, for a forging force of 55 N and with the parallelepiped-shaped hammer, some of the pores were fully collapsed.

The feasibility of the new HF-WAAM variant in promoting grain refinement and pore collapse is demonstrated in this work. It is expected, but needs to be confirmed in future work if this novel WAAM variant impact the microstructure in the deposited materials and also its influence on the fatigue behavior of structural parts produced by HF-WAAM.

5. Conclusions

This paper presents a new variant of WAAM and the physical and metallurgical principles which it is based on; this variant is named HF-WAAM and is based on hot forging between deposited layers.

A customized WAAM torch was developed, manufactured, and

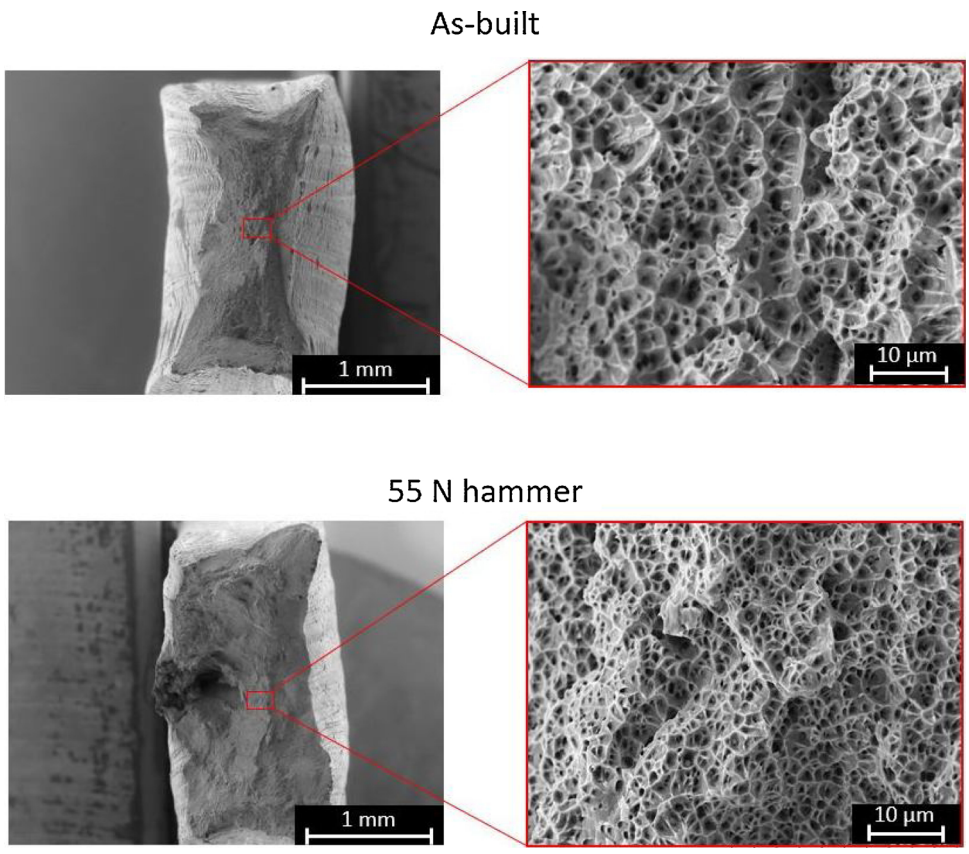

Fig. 15. Fracture surface from uniaxial tensile test specimen for the as-built (top) and 55 N hammer (bottom).

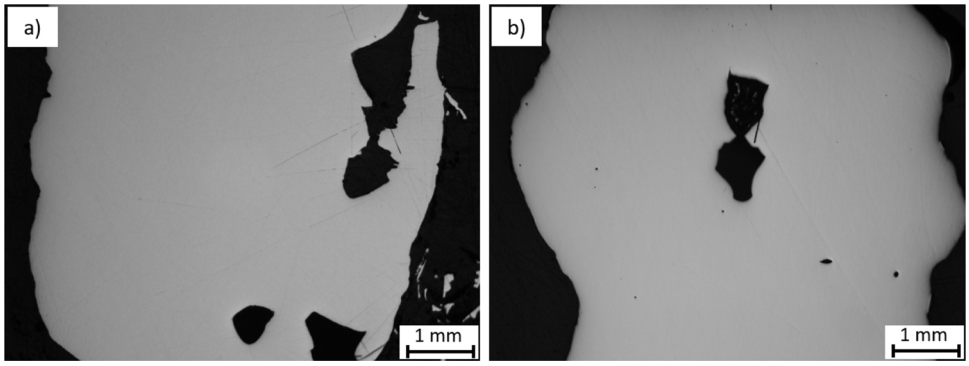

Fig. 16. Optical images of the as-built sample without shielding gas.

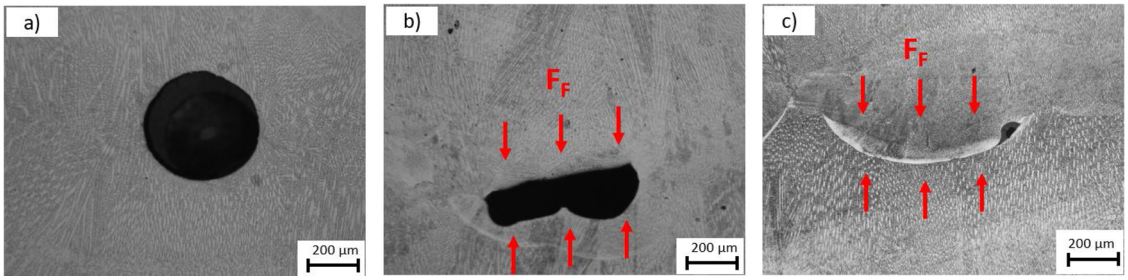

Fig. 17. Evaluation of porosity for a) 17 N forging, b) 55 N forging, and c) 55 N forging with reduced area.

tested.

This variant showed potential for industrial applications with advantages in terms of the following:

Equipment used. Because the deformation occurs at high temperatures, the forces involved are small, and the stiffness of the hot forging equipment is lower than that of the cold rolling variant [20]. Thus, the hot forging variant can be incorporated into conventional

moving equipment used in WAAM such as XYZ table or 6-axis robot. Because the forces are small, the energy consumed is almost negligible, which is an additional valuable benefit.

Integrity and strength of the parts. The hot forging effect refines the solidification microstructure, thereby improving the mechanical strength. Compared to as build part, the yield strength increased from 360 to 450 MPa, ultimate tensile strength improved from 574 to 622, while elongation to fracture reduced from 32 to 28 %. Additionally, existent internal pores collapsed under the forging force, which is beneficial for the behavior in-service of additive manufactured parts.

Declaration of Competing Interest

All authors have participated in (a) conception and design, or analysis and interpretation of the data; (b) drafting the article or revising it critically for important intellectual content; and (c) approval of the final version.

This manuscript has not been submitted to, nor is under review at, another journal or other publishing venue.

The authors have no affiliation with any organization with a direct or indirect financial interest in the subject matter discussed in the manuscript

Acknowledgments

Authors acknowledge Fundação para a Ciência e a Tecnologia (FCT - MCTES) for its financial support via the project UID/EMS/00667/2019 (UNIDEMI). VD acknowledges FCT - MCTES for funding the PhD grant SFRH/BD/139454/2018. TAR acknowledges FCT - MCTES for funding the PhD grant SFRH/BD/144202/2019. This activity has received funding from the European Institute of Innovation and Technology (EIT). This body of the European Union receives support from the European Union's Horizon 2020 research and innovation programme. Parts of this research were carried out at PETRA III at DESY, a member of the Helmholtz Association. The research leading to this result has been supported by the project CALIPSOplus under the Grant Agreement 730872 from the EU Framework Programme for Research and Innovation HORIZON 2020. This project has received funding from the EU-H2020 research and innovation programme under grant agreement No 654360 having benefitted from the accessprovided by PETRA III at DESY in Hamburg, Germany within the framework of the NFFA-Europe Transnational Access Activity.

Appendix A. Supplementary data

Supplementary material related to this article can be found, in the online version, at doi:https://doi.org/10.1016/j.addma.2020.101193.

References

[1] T. DebRoy, H.L. Wei, J.S. Zuback, T. Mukherjee, J.W. Elmer, J.O. Milewski, A.M. Beese, A. Wilson-Heid, A. De, W. Zhang, Additive manufacturing of metallic components – process, structure and properties, Prog. Mater. Sci. 92 (2018) 112–224, https://doi.org/10.1016/j.pmatsci.2017.10.001.

[2] J.P. Oliveira, T.G. Santos, R.M. Miranda, Revisiting fundamental welding concepts to improve additive manufacturing: from theory to practice, Prog. Mater. Sci. (2019) 100590, https://doi.org/10.1016/J.PMATSCI.2019.100590.

[3] T.A. Rodrigues, V. Duarte, R.M. Miranda, T.G. Santos, J.P. Oliveira, Current status and perspectives on wire and arc additive manufacturing (WAAM), Materials (Basel) 12 (2019) 1121, https://doi.org/10.3390/ma12071121.

[4] J. Gu, J. Ding, S.W. Williams, H. Gu, P. Ma, Y. Zhai, The effect of inter-layer cold working and post-deposition heat treatment on porosity in additively manufactured aluminum alloys, J. Mater. Process. Technol. 230 (2016) 26–34, https://doi.org/10.1016/J.JMATPROTEC.2015.11.006.

[5] A. Lopez, R. Bacelar, I. Pires, T.G. Santos, J.P. Sousa, L. Quintino, Non-destructive testing application of radiography and ultrasound for wire and arc additive manufacturing, Addit. Manuf. 21 (2018) 298–306, https://doi.org/10.1016/J.ADDMA.2018.03.020.

[6] Y. Javadi, C.N. MacLeod, S.G. Pierce, A. Gachagan, D. Lines, C. Mineo, J. Ding, S. Williams, M. Vasilev, E. Mohseni, R. Su, Ultrasonic phased array inspection of a Wire + Arc Additive Manufactured (WAAM) sample with intentionally embedded defects, Addit. Manuf. 29 (2019) 100806, , https://doi.org/10.1016/j.addma.2019.100806.

[7] A. Chabot, N. Laroche, E. Carcreff, M. Rauch, J.Y. Hascoët, Towards defect monitoring for metallic additive manufacturing components using phased array ultrasonic testing, J. Intell. Manuf. (2019) 1–11, https://doi.org/10.1007/s10845-019-01505-9.

[8] P.A. Colegrove, F. Martina, M.J. Roy, B.A. Szost, S. Terzi, S.W. Williams, P.J. Withers, D. Jarvis, High Pressure Interpass Rolling of Wire + Arc Additively Manufactured Titanium Components, (2014), https://doi.org/10.4028/www.scientific.net/AMR.996.694.

[9] H.O. Zhang, W. Rui, L. Liye, G.L. Wang, HDMR technology for the aircraft metal part, Rapid Prototyp. J. 22 (2016) 857–863, https://doi.org/10.1108/RPJ-05-2015-0047.

[10] Y. Xie, H. Zhang, F. Zhou, Improvement in geometrical accuracy and mechanical property for arc-based additive manufacturing using metamorphic rolling mechanism, J. Manuf. Sci. Eng. 138 (2016) 111002, , https://doi.org/10.1115/1.4032079.

[11] M.P. Sealy, G. Madireddy, R.E. Williams, P. Rao, M. Toursangsaraki, Hybrid processes in additive manufacturing, J. Manuf. Sci. Eng. 140 (2018) 060801, , https://doi.org/10.1115/1.4038644.

[12] M.C. Flemings, Behavior of metal alloys in the semisolid state, Metall. Trans. A 22 (1991) 957–981, https://doi.org/10.1007/BF02661090.

[13] J.P. Oliveira, F.M.B. Fernandes, R.M. Miranda, N. Schell, J.L. Ocaña, Residual stress analysis in laser welded NiTi sheets using synchrotron X-ray diffraction, Mater. Des. 100 (2016) 180–187, https://doi.org/10.1016/j.matdes.2016.03.137.

[14] D. Samantaray, S. Mandal, A.K. Bhaduri, S. Venugopal, P.V. Sivaprasad, Analysis and mathematical modelling of elevated temperature flow behaviour of austenitic stainless steels, Mater. Sci. Eng. A 528 (2011) 1937–1943, https://doi.org/10.1016/J.MSEA.2010.11.011.

[15] Y. Lee, M. Nordin, S.S. Babu, D.F. Farson, Effect of fluid convection on dendrite arm spacing in laser deposition, Metall. Mater. Trans. B 45 (2014) 1520–1529, https://doi.org/10.1007/s11663-014-0054-7.

[16] X. Chen, J. Li, X. Cheng, B. He, H. Wang, Z. Huang, Microstructure and mechanical properties of the austenitic stainless steel 316L fabricated by gas metal arc additive manufacturing, Mater. Sci. Eng. A 703 (2017) 567–577, https://doi.org/10.1016/J.MSEA.2017.05.024.

[17] T.A. Rodrigues, V. Duarte, J.A. Avila, T.G. Santos, R.M. Miranda, J.P. Oliveira, Wire and arc additive manufacturing of HSLA steel: effect of thermal cycles on microstructure and mechanical properties, Addit. Manuf. 27 (2019) 440–450, https://doi.org/10.1016/J.ADDMA.2019.03.029.

[18] Z. Wang, T.A. Palmer, A.M. Beese, Effect of processing parameters on microstructure and tensile properties of austenitic stainless steel 304L made by directed energy deposition additive manufacturing, Acta Mater. 110 (2016) 226–235, https://doi.org/10.1016/j.actamat.2016.03.019.

[19] B.P. Kashyap, K. Tangri, On the Hall-Petch relationship and substructural evolution in type 316L stainless steel, Acta Metall. Mater. 43 (1995) 3971–3981, https://doi.org/10.1016/0956-7151(95)00110-H.

[20] F. Martina, P.A. Colegrove, S.W. Williams, J. Meyer, Microstructure of interpass rolled wire + arc additive manufacturing Ti-6Al-4V components, Metall. Mater. Trans. A 46 (2015) 6103–6118, https://doi.org/10.1007/s11661-015-3172-1.